Micromechanical Pierce Oscillator for Resonant Sensing Applications

Ashwin A. Seshia*, Wing Zin Low*, Sunil A. Bhave*, Roger T. Howe* and Stephen Montague†

*Berkeley Sensor & Actuator Center, 497 Cory Hall, Dept. of Electrical Engineering and Computer Sciences, University of California, Berkeley, CA 94720, USA.
†Sandia National Laboratories, Albuquerque, NM 87185, USA.

ABSTRACT

We present the design techniques and experimental characterization of a Pierce oscillator circuit adapted for micromechanical elements with resonant frequencies lying between 100 and 300 kHz. Micromechanical double-ended tuning fork resonators serve as the crystal element of the oscillator. The measured phase noise of these oscillators lies below -100 dBc/Hz at a frequency offset of 500 Hz away from the carrier with in-circuit quality factors exceeding 30000. This noise figure improves upon previous reported values and demonstrates the feasibility of a Pierce oscillator for micromechanical vibrating elements with resonant frequencies lying under 1 MHz. The value of the second harmonic distortion factor (HD_2) is -44 dB for an output amplitude of 50 mV.

***Keywords*:** micromechanical oscillator, resonator, resonant sensing, Pierce circuit.

INTRODUCTION

Micromechanical oscillators have been considered as attractive replacements for quartz crystal oscillators as timing references in digital circuits due their small size and potential for fabrication compatibility with standard CMOS VLSI processes, enabling novel single chip systems. In addition, micromechanical oscillators form essential components of many transducers such as accelerometers [1], gyroscopes, pressure sensors, AFM probes and biological sensors to detect molecular interactions. The performance of the oscillator is critical in all of these applications and is often a limiting factor in overall system performance.

The primary design challenge of adapting an oscillator circuit for thin-film micromechanical resonating elements is the large equivalent motional resistance of the resonating element. Early work in micromechanical oscillators employed transresistance amplifiers [2] to supply the high gain required to sustain oscillation in micromechanical elements. Recently, lower noise oscillator topologies such as the Pierce scheme [3,4] have been demonstrated.

This paper discusses the design techniques involved in adapting the Pierce oscillator scheme for micromechanical resonating elements. Experimental verification of these design principles has been conducted for micromechanical double-ended tuning fork (DETF) resonators with resonant frequencies lying between 100 and 300 kHz. DETF oscillators in this frequency regime are often incorporated as sense elements in resonant accelerometers and gyroscopes. The performance of the oscillator directly determines the resolution of the sensor and hence a low noise oscillator configuration is essential.

OSCILLATOR DESIGN

The micromechanical oscillator comprises of a free-standing element (a double-ended tuning fork in the current implementation) configured to resonate in a desired mode. A schematic of the double-ended tuning fork is shown in Figure 1. The electromechanical characteristics of the resonating element can be described by an electrical equivalent composed of a series LCR circuit [2]. The parasitic feedthrough capacitor (C_o), that may have sources in substrate coupling or poor layout, couples the drive voltage over to the port where the motional current is sensed**.** This parasitic feedthrough capacitor (C_o) serves to introduce a phase shift in the loop and can thereby degrade oscillation.

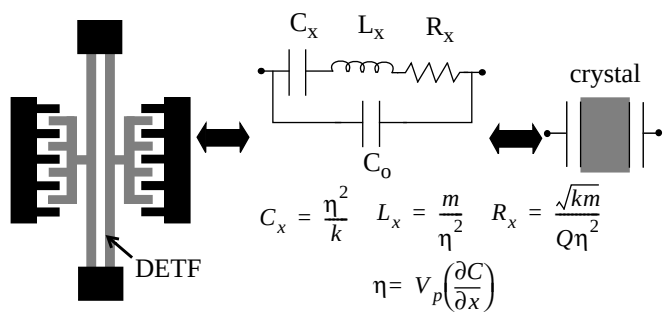

Figure 1: Schematic of the mechanical structure of the double-tuning fork and its simplest electrical equivalent circuit.

As shown in Figure 2 (A), the electromechanical element is embedded in the feedback loop of a sustaining amplifier. The Pierce oscillator topology uses a capacitive input to integrate the motional current from the resonator. A DC biasing path to the amplifier input is provided by a large resistor. The value of this resistor should be set large enough so as to not introduce significant loading at the amplifier input or additional phase shift in the signal path. The gate

capacitance of the active input device must be designed to be much smaller than the integrating capacitance to avoid amplitude fluctuations due to large drive voltages. The device sizes and bias conditions are determined by optimizing with respect to a trade-off involving the oscillator signal-to-noise ratio, output distortion and amplifier gain. The condition for oscillation can be written in terms of the loop gain ($G(j\omega)$):

$$\angle G(j\omega) = 0^\circ$$
$$|G(j\omega)| \geq 1 \qquad ...(1)$$
$$G(j\omega) = \frac{G_m Z_1 Z_2}{Z_1 + Z_2 + Z_{xtal}}$$

For a high-Q oscillator, the resonant characteristics of the mechanical element should define the output frequency. The Pierce circuit operates at a frequency slightly higher than the actual series resonance frequency where the crystal acquires an inductive behavior ($Z_{xtal} = j\omega L_{eff} + R_x$). The motional resistance (R_x) degrades the oscillator loop gain and for large enough values can prevent oscillator startup. Figure 3 depicts how the loop gain degrades as a function of the high equivalent motional resistance of these resonators.

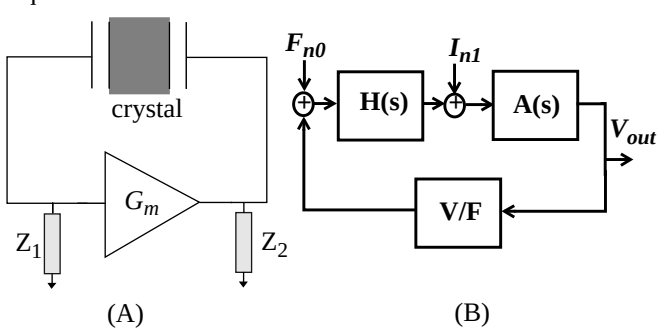

Figure 2: Schematic of the Pierce oscillator circuit. (A) is a block diagram of the circuit while (B) is the linear system equivalent. A(s) is the amplifier transfer function and H(s) is the mechanical transfer function.

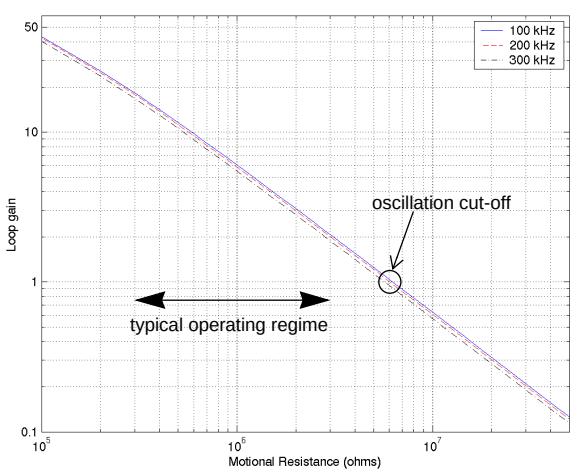

Figure 3: Plot of the magnitude of the maximum loop gain as a function of the motional resistance of the resonator at different oscillator output frequencies.

Figure 2 (B) shows a schematic of the Pierce oscillator, including its simplest representation as a linear system. The relevant transfer functions can be written as a function of the frequency spacing from the carrier ($\Delta\omega$):

$$\left|\frac{V_{out}}{F_{n0}}\right| = \left|\frac{A\eta}{2m}\frac{j}{\Delta\omega}\right| \qquad ...(2)$$
$$\left|\frac{V_{out}}{I_{n1}}\right| = \left|A + \frac{Aj\omega_o}{2Q\Delta\omega}\right| \qquad ...(3)$$

A is the gain supplied by the sustaining amplifier to overcome the motional resistance loss in the mechanical element. These equations are relevant for the noise analysis where I_{n1} represents the equivalent current noise injected at the input of the sustaining amplifier and F_{n0} is the noise equivalent force that the mechanical element is subjected to as a result of the brownian motion of the gas particles in the surrounding ambient [5].

The distortion in the oscillator output can arise due to a number of different reasons. At large drive voltages, the small signal model of the active input device of the amplifier is no longer valid and the gain of the input device begins to change as it moves out of the desired bias region and possibly from saturation into triode. In addition, there could be mechanical nonlinearities due to overdrive as the spring constant exhibits a stiffening effect, electrostatic nonlinearities due to non-ideal actuators and sensing mechanisms that introduce transduction coefficients that are amplitude dependent.

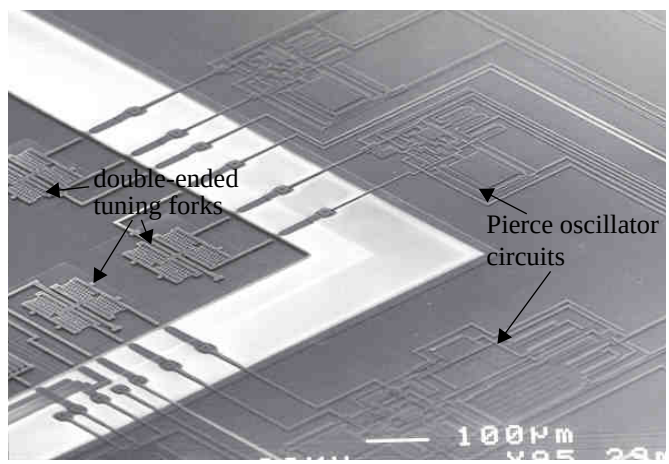

Figure 4: SEM of three double-ended tuning fork oscillators of differing output frequencies fabricated in the Sandia integrated MEMS process.

EXPERIMENTAL VERIFICATION OF OSCILLATOR MODEL

An SEM of the array of devices fabricated in the Sandia National Laboratories integrated MEMS process [6] is shown in Figure 4. The double-ended tuning forks are designed with resonant frequencies lying between 100 kHz and 300 kHz. A single stage sustaining amplifier is designed in the standard Pierce configuration (Figure 5). High imped-

ance biasing of the input node of the amplifier is implemented by MOS transistors biased in the subthreshold region of operation. The single-stage amplifier provides sufficient gain to allow for the equivalent series resistance of the DETF element to be as high as 5MΩ. This allows for operation of these devices in ambient pressures under 250 mtorr.

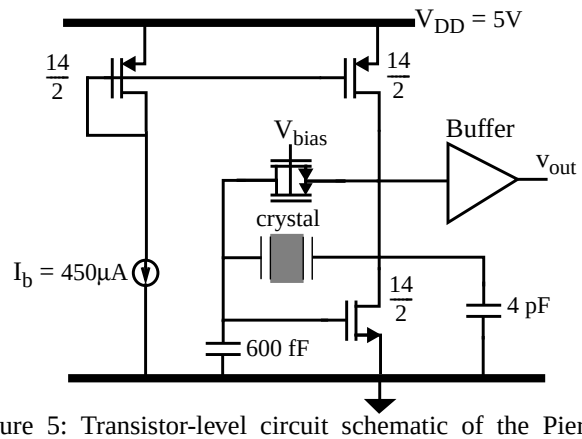

Figure 5: Transistor-level circuit schematic of the Pierce oscillator. The crystal block represents the electrical equivalent of the double-ended tuning fork structure.

Figure 6 is an experimentally measured plot of the power spectrum of the oscillator output over a 6 kHz range centered around the carrier frequency. A linearized model of the oscillator predicts that the background noise level away from the carrier is limited by the electronic noise of the sustaining amplifier. Background noise estimates from theory, backed by SPICE simulation, match closely with values obtained by experiment. At frequencies near the carrier, the relationship between the noise power and the frequency spacing from the carrier (Figure 7) follows an inverse cubic power law relationship. This behavior indicates an aliasing of the 1/f noise from the amplifier onto the carrier frequency. A possible explanation of this behavior is a noise current injected at the input of the amplifier resulting from the mixing of the amplifier 1/f noise with the resonator displacement. The phase noise expression for this behavior is given by:

$$\mathcal{L}(f_m) = 10\log\left(\left(\frac{f_o}{2QV_p}\right)^2 \frac{K_f}{WLC_{ox}f_m^3}\right) \quad ...(4)$$

where f_m is the frequency spacing from the carrier and f_o is the nominal resonant frequency of the DETF. Away from the carrier the noise floor is set by the thermal electronic noise of the sustaining amplifier. This noise expression is given by:

$$\mathcal{L}(f_m) = 10\log\left(\frac{4k_BTA_v^2}{\overline{v_o^2}}\frac{2}{3g_{mt}}\right) \quad ...(5)$$

Here $\overline{v}_o$ is the output rms voltage of the oscillator and g_{mt} is an equivalent transconductance considering the thermal noise contribution of all the transistors in the sustaining amplifier.

The output of the oscillator exhibits a second harmonic distortion factor (HD_2) of -44 dB for an output amplitude of 50 mV. The value of HD_2 is directly proportional to the output amplitude of the oscillator as expected for nonlinearities that can be expressed as a sum of higher order harmonics of the resonator displacement. At this point, investigation into the source of the distortion is still ongoing but it is likely that the nonlinearity of the capacitive transduction scheme to measure the motional current dominates. Higher harmonics in the drive force are filtered by the mechanical transfer function of the resonator and spring stiffening resulting from large resonator displacements would result in a third harmonic peak. MOS device nonlinearities are minimal as the drive voltages used are fairly low. Nonlinearities due to damping could be a potential cause but are difficult to model accurately for this geometry.

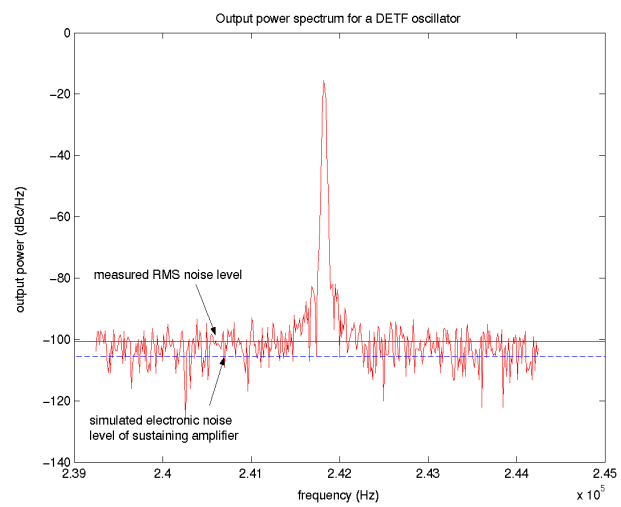

Figure 6: Output power spectrum of a 241.9 kHz double-ended tuning fork oscillator.

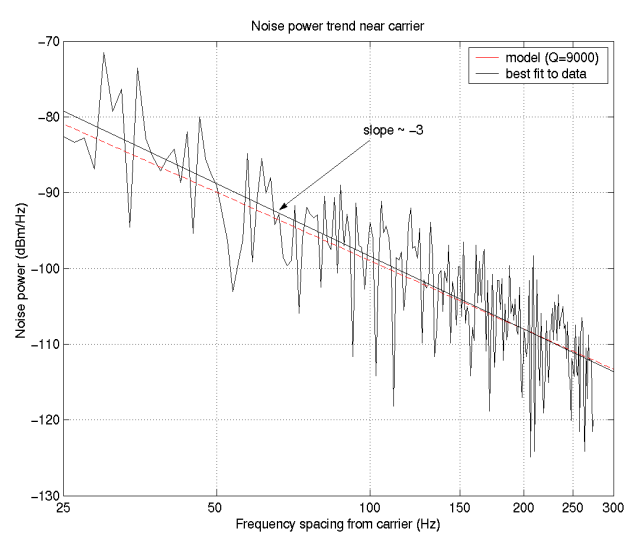

Figure 7: The noise trend of the oscillator near the carrier frequency. Note the $1/f^3$ dependence of the noise power.

Finite element simulations were used to model the capacitance gradient for a comb drive structure (Figure 8). The nonlinearity in the capacitance gradient can be expressed as a power series function of the resonator displacement.

$$\frac{\partial C}{\partial x} = a_o + a_1 x + a_2 x^2 + \ldots \qquad ...(6)$$

$$i_s = V_p \cdot \omega_o x\left(\frac{\partial C}{\partial x}\right) + v_1 \omega_o x\left(\frac{\partial C}{\partial x}\right) \qquad ...(7)$$

The resulting expression for HD_2 is given by:

$$HD_2 = 20\log\left(\frac{a_1 x}{a_o}\right) \qquad ...(8)$$

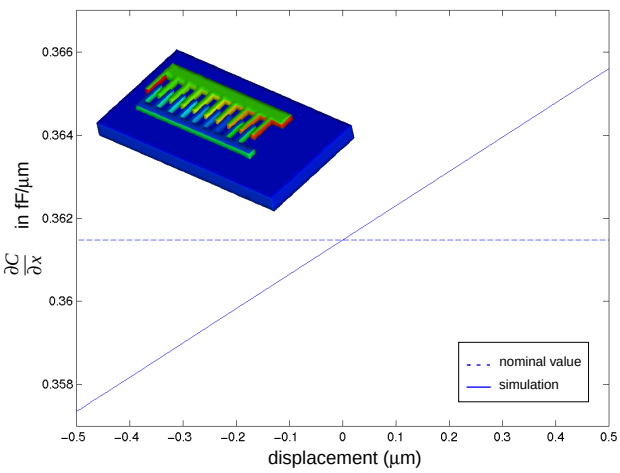

Figure 8: Plot of the capacitance gradient along the direction of motion as a function of comb finger overlap for an estimated range of motion of 1µm obtained using MEMCAD. The error of the fit to the data is less than 0.015%.

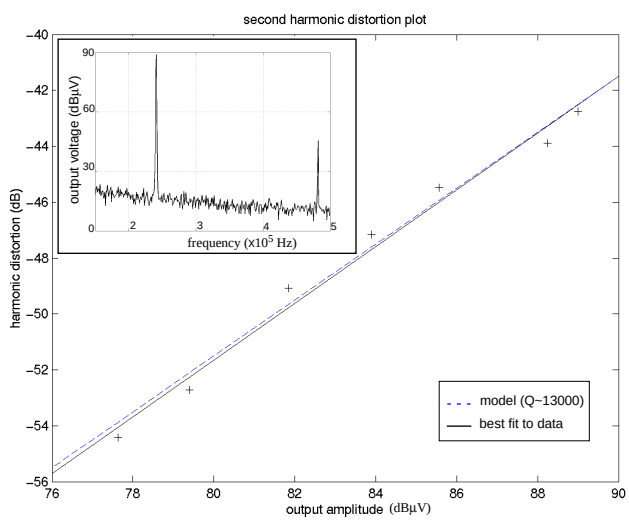

Figure 9: Appearance of the second harmonic peak in the oscillator output shown in the inset. Note the near linear relationship in the least squares fit for HD_2 as expected. The dashed line shows the predicted HD_2 obtained by considering the capacitance gradient nonlinearity.

The second term in equation (7) represents a mixing of the resonator displacement with the amplifier input voltage but the estimated power of the second harmonic peak due this term is an order of magnitude lower. The linear relationship between the output amplitude and the magnitude of HD_2 is verified experimentally (Figure 9). The predicted value of HD_2 obtained from results of the finite element simulation to model the comb drive nonlinearity agree with experiment.

SUMMARY

A micromechanical Pierce oscillator was designed and implemented in the Sandia National Laboratories IMEMS process. The noise floor of the device at a frequency spacing of 500 Hz away from the carrier is less than -100 dBc/Hz, limited by the electronic noise of the sustaining amplifier. The noise power behavior close to the carrier follows a $1/f^3$ trend that matches well with a model indicating a mixing of the 1/f noise from the amplifier onto the carrier frequency. The second harmonic distortion factor of the oscillator is about -44 dB for an output amplitude of 50 mV and seems to arise due to the nonlinearity of the comb drive transducer used to measure the motional current.

ACKNOWLEDGEMENTS

The work was partially supported by DARPA grants F30602-97-2-0266 and F30602-97-C-0127. The devices were fabricated at Sandia National Laboratories. Thanks go to Ron Wilson for the SEM work and to Trey Roessig for discussions on oscillator noise.

REFERENCES

[1] T. Roessig et al., Surface-micromachined resonant accelerometer, Ninth International Conference in Solid State Sensors and Actuators, 1997, pp. 859-862.

[2] C. Nguyen et al., An Integrated CMOS Micromechanical Resonator High-Q Oscillator, *IEEE Journal of Solid State Circuits*, Vol. 34, No. 4, April 1999, pp. 440-455.

[3] T. Roessig et al., Surface-Micromachined 1MHz Oscillator With Low-Noise Pierce Configuration, Proc. Solid State Sensors and Actuators Workshop, Hilton Head 1998, pp. 328-332.

[4] S. Lee et al., A 10-MHz Micromechanical Resonator Pierce Reference Oscillator for Communications, Proc. Eleventh International Conference in Solid State Sensors and Actuators, 2001, pp. 1094-7.

[5] T. Gabrielson et al., Mechanical-thermal noise in micromachined acoustic and vibration sensors, *IEEE Transactions on Electron Devices*, vol.40, no.5, May 1993, pp. 903-9.

[6] J. Smith et al., Embedded micromechanical devices for the monolithic integration of MEMS with CMOS, *IEDM Tech. Digest*, 1995, pp. 609-612.